Highlights

Scale-dependent coupling between galactic cosmic rays and trace gases revealed by multifractal analysis

D. Sierra-Porta

- MFDFA/MFDCCA reveal scale-dependent GCR–gas coupling
- CH4 shows the widest multifractal spectrum; O3 is intermediate
- Cosmic rays leave a subtle, scale-selective fingerprint on trace gases

Scale-dependent coupling between galactic cosmic rays and trace gases revealed by multifractal analysis

D. Sierra-Porta[a,]

[a] *Universidad Tecnológica de Bolívar. Escuela de Transformación Digital., Parque Industrial y Tecnológico Carlos Vélez Pombo Km 1 Vía Turbaco., Cartagena de Indias, 130010, Colombia*

Abstract

Galactic cosmic rays (GCR) modulate atmospheric ionisation and may influence reactive greenhouse gases, yet linear correlations have proved inconclusive. We analyse 74 328 hourly observations (2016–2024) of pressure-corrected neutron-monitor counts and co-located CH_4 and O_3 mixing ratios from the high-alpine Jungfraujoch station using Multifractal Detrended Fluctuation Analysis (MFDFA) and its bivariate extension (MFDCCA). Cosmic rays exhibit a narrow, quasi-monofractal singularity spectrum ($\Delta\alpha_{\text{full}} = 0.43$), consistent with heliospheric modulation as a single dominant driver, whereas O_3 and CH_4 display progressively broader spectra ($\Delta\alpha = 0.78$ and 0.84). Cross-Hurst exponents exceed unity for small-to-moderate fluctuations, indicating super-persistent joint variability on 1–7 d (O_3) and 7–30 d (CH_4) horizons—time-scales compatible with HO_x/NO_x chemistry triggered by GCR ionisation. Quadratic fits to the cross-singularity spectra yield half-maximum widths of 0.39 (CH_4–GCR) and < 0.33 (O_3–GCR), quantifying a broader amplitude hierarchy for methane. Extreme gas anomalies, by contrast, show weak cross persistence, implicating dynamical intrusions rather than ionisation. Multifractal metrics thus expose a scale-selective GCR imprint masked in Pearson and Spearman statistics and suggest that incorporating GCR flux as a multiscale covariate could improve sub-monthly O_3/CH_4 predictions. The approach provides a transferable framework for disentangling cosmic-ray forcing from chemical and dynamical controls in other trace-gas records.

Keywords:
2000 MSC: 70K55, 85A35, 85A20, 86A10, 37A60
galactic cosmic rays, methane, ozone, multifractal analysis, atmospheric ionisation, space weather, trace-gas variability

1. Introduction

Galactic cosmic rays (CRs)—relativistic nuclei and electrons accelerated in supernova remnants, pulsar magnetospheres and other high-energy astrophysical sites—impinge continuously on Earth's atmosphere. Their hadronic cascades convert a small fraction of the atmospheric column into a dense swarm of secondary particles (muons, neutrons, pions, ...) whose sea-level

*Corresponding author: Email address: dporta@utb.edu.co (D. Sierra-Porta)
**Orcid: 0000-0003-3461-1347 (D. Sierra-Porta)
Email address: dporta@utb.edu.co (D. Sierra-Porta)

footprint responds both to heliospheric modulation and to local thermodynamic conditions (Donnini, 2021; Riádigos et al., 2022; Utomo, 2017). Seasonal and synoptic variations in tropospheric temperature alter meson decay and attenuation lengths, imprinting a measurable temperature effect on muon and neutron monitors (Jeong and Oh, 2020; Maghrabi et al., 2015, 2023). Superimposed on this meteorological forcing, the 11- and 22-year solar cycles modulate CR fluxes with lags of a few to ∼14 months that depend on particle rigidity and solar magnetic polarity (Tomassetti et al., 2022; Gong et al., 2025).

Beyond their utility as geophysical probes, CRs initiate ion-molecule chemistry that can perturb key oxidative and radiative tracers. Ion pairs produced in the middle atmosphere trigger fast reactions—up to ten orders of magnitude faster than neutral–neutral pathways—that enhance HO_x and NO_x abundances (Catone et al., 2023; Satta et al., 2024). The ensuing catalytic cycles destroy ozone and elevate hydroxyl radicals, thereby shortening the lifetime of methane (Naik et al., 2013; Brune et al., 2020). Global-chemistry simulations demonstrate that persistent GCR backgrounds reduce lower-stratospheric O_3 by $\gtrsim$10 % and can draw down CH_4 by tens of percent under extreme flux scenarios (Matthes et al., 2017; Tabataba-Vakili et al., 2016). Yet observational verification remains elusive because both CR and gas records exhibit strong trends, long-range persistence, and multiple characteristic time scales.

Ionisation rates peak near the Pfotzer maximum at ∼15–18 km, where Galactic CRs deposit $O(10^4)$ eV g^{-1} s^{-1} into the air column (Meng et al., 1997; Schnadt et al., 2002; Jackman et al., 2007, 2005). Each ion pair yields, on average, 1.2 reactive OH radicals and ∼1.6 HO_2 radicals via hydration of the primary ion cluster $H_2O^+ \cdot (H_2O)_n$ and subsequent proton transfer reactions (Seinfeld and Pandis, 2016). In parallel, impact excitation of N_2 produces $N(^2D)$ atoms that react with O_2 to form NO, seeding the NO_x cycle (Calisto et al., 2011). The coupled HO_x–NO_x system drives two feedback loops: *(a)* NO catalytically destroys O_3 through the classic $NO + O_3 \rightarrow NO_2 + O_2$ / $NO_2 + h\nu \rightarrow NO + O$ pathway; and *(b)* elevated OH shortens the CH_4 lifetime via $CH_4 + OH \rightarrow CH_3 + H_2O$, thereby lowering CH_4 concentrations and further altering odd-hydrogen budgets (Prather and Hsu, 2010; Naik et al., 2013). Model studies show that a 10 % increase in ionisation can raise the zonal-mean OH column by 2–4 %, translating into a 1–2 % decrease in CH_4 and a concomitant ∼1 DU (Dobson Unit) ozone loss in the lower stratosphere (Jackman et al., 2016; Scheucher et al., 2018; Grenfell et al., 2007, 2012).

Altitude and latitude modulate the sign of these responses. In cold, low-NO_x air masses above Antarctica, CR-induced NO_x can actually enhance O_3 by suppressing halogen-catalysed loss, whereas within the chlorine-rich Arctic vortex the same mechanism amplifies O_3 depletion (Calisto et al., 2011). Tropospheric CH_4 responds on multi-week time scales set by vertical mixing and OH regeneration, whereas stratospheric O_3 can react within days as NO descends from the mesosphere after solar proton events (Maliniemi et al., 2021; Konopka et al., 2007; Portmann et al., 2012). These chemically distinct latency windows—∼1–7 days for O_3 versus ∼7 30 days for CH_4—provide physically motivated benchmarks against which to interpret the scale-resolved MFDCCA spectra derived below. High-altitude stations provide the cleanest natural laboratories for such tests. Jungfraujoch (3580 m.a.s.l.) offers continuous, in-situ monitoring of CR counts alongside near-background CH_4 and O_3 concentrations. Because the site sits above much of the planetary boundary layer, it minimises confounding anthropogenic variability while retaining sensitivity to ionisation changes in the lower stratosphere and upper free troposphere.

Ionisation does more than seed HO_x/NO_x chemistry; it also changes the microphysical budget of cloud condensation nuclei (CCN). Charged molecular clusters containing H_2SO_4, NH_3 and organics grow more efficiently than neutral clusters, enhancing new-particle formation rates by up to an order of magnitude under clean-marine conditions (Kirkby et al., 2011; Pierce, 2017).

Observational studies during the 1980s–1990s reported a positive correlation between low-cloud cover and galactic CR flux (Svensmark and Friis-Christensen, 1997; Friis-Christensen and Svensmark, 1997; Marsh and Svensmark, 2000), although the signal weakened in the 2000s and remains debated (Miyahara et al., 2023; Harrison et al., 2015). Even if the radiative impact is small, the CR–CCN link is relevant here because increases in CCN modulate aqueous-phase production of HO_2 and alter photolysis rates within cloudy columns (Carslaw et al., 2002). Hence cloud-mediated feedbacks provide an additional, albeit indirect, avenue through which CR variability can influence the budgets of O_3 and CH_4—reinforcing the motivation to search for multifractal fingerprints of cosmic rays in these gases.

Recent analyses using satellite and reanalysis products report additional evidence and mixed signals on CR–cloud couplings. For the Eastern Mediterranean, Christodoulakis et al. (2019) examined satellite cloud parameters versus CR proxies and discussed regional dependencies, while Pierce (2017) synthesised CLOUD results on ion-mediated nucleation and implications for cloud microphysics. Extending to broader temporal context, Varotsos et al. (2024) investigated the time evolution of cosmic rays in a new time domain, which can help define objective event windows for testing atmospheric responses. Together, these studies underscore both the opportunities and challenges in isolating CR fingerprints in clouds and precipitation.

Recent observational work has continued to probe possible CR–cloud–precipitation couplings. Using satellite products, (Varotsos et al., 2023b) reported statistical links between rain, cloud fields and galactic cosmic rays, adding to the mixed body of evidence on the sign and robustness of CR–cloud associations. In parallel, methodological advances on the space-weather side have proposed nowcasting schemes for extreme CR events (Varotsos et al., 2023a), which—while focused on particle environment monitoring—could help frame cause–effect tests by providing objective event onsets and amplitudes against which atmospheric responses might be evaluated. These studies reinforce both the opportunities and the challenges in isolating a CR fingerprint on clouds and hydrological variables, motivating multiscale diagnostics that can discriminate amplitude classes and time windows.

Classical Pearson or Fourier diagnostics struggle to disentangle scale-dependent, non-stationary correlations between CRs and chemically active gases. Multifractal Detrended Fluctuation Analysis characterises the internal scaling hierarchy of a single time series, whereas its bivariate extension, MFDCCA, quantifies scale-resolved coupling between paired records—even in the presence of strong trends or non-Gaussian noise. These techniques have already exposed hidden links between sunspots and CR fluctuations (Sierra-Porta, 2022, 2025). Here we extend the approach to atmospheric chemistry, asking whether the multifractal signatures of O_3 and CH_4 variability at Jungfraujoch encode a detectable imprint of CR modulation.

This study seeks to (i) quantify the multifractal structure of hourly CR, O_3, and CH_4 series at Jungfraujoch during 2016–2024 and (ii) evaluate whether scale-dependent cross-correlations among these variables align, in amplitude and lag, with ion-chemistry expectations. Because O_3 should respond to HO_x/NO_x perturbations on 1–7-day horizons and CH_4 on 7–30-day horizons, we interpret the MFDCCA spectra against these chemically motivated windows to assess causal plausibility. Our results provide a physically grounded test of the long-postulated CR influence on greenhouse-relevant gases and deliver a multifractal baseline for future process-resolving models.

2. Materials and Methods

2.1. Data

This study exploits the co-located, high-altitude observations from the Global Atmosphere Watch (GAW) site at Jungfraujoch (46.55° N, 7.98° E; 3580 m.a.s.l.). Hourly cosmic-ray counts are provided by the University of Bern neutron monitor (cut-off rigidity ≈ 4.5 GV). Raw data are available from the Neutron Monitor Database (NMDB) and NEST official release: https://nest.nmdb.eu. (accessed on: April 2025). The monitor's raw counts were pressure-corrected with the station barometer and expressed as counts h^{-1}. The observational record extends from 01:00 UTC on 1 January 2016 to 00:00 UTC on 1 July 2024, supplying almost eight and a half years of continuous hourly measurements for all three variables.

Except for a handful of clearly spurious points, the cosmic-ray series remains in its raw form. Hourly values that exceeded the long-term mean by more than ten standard deviations—isolated bursts attributable to detector malfunctions on a few specific days—were removed (< 0.2 % of the record). Short gaps created by this culling and by occasional acquisition outages were infilled with linear interpolation confined to gaps shorter than three consecutive hours. After this minimalist cleaning, the series contains 74 328 non-null observations out of the original 74 465, preserving both the statistical structure and the natural variability of the data set. Missing segments were reconstructed with the *iterative imputation* strategy of `scikit-learn` (Nikfalazar et al., 2020; Holt and Benfer Jr, 2000). In each iteration, a random-forest regressor (200 trees, maximum depth unrestricted, bootstrap enabled) predicted the missing value of a target timestamp from the complete contemporaneous values. The procedure converged within five passes, and out-of-bag errors confirmed that imputed points fall well inside the natural spread of the hourly series. Consequently, the final cosmic-ray record retains 74 328 valid data points while minimising artefacts introduced by gap filling. We chose iterative random-forest imputation because it captures possible nonlinear relations among co-measured variables without imposing parametric forms and is robust to outliers and interactions; the imputed fraction is < 0.2% of the grid, and out-of-bag errors confirm negligible bias relative to the native spread.

Across the 74 465 hourly cosmic-ray measurements, the monitor records a mean intensity of 161.79 counts h^{-1} with a standard deviation of 5.42 counts h^{-1}, yielding a coefficient of variation of only 3.3 %, indicative of the relatively stable background flux expected at Jungfraujoch. The central tendency is framed by a median of 163.87 counts h^{-1}; the inter-quartile range spans from 159.16 (25th percentile) to 165.77 counts h^{-1}, while the full observed range extends from a minimum of 144.01 to a maximum of 171.04 counts h^{-1}. These statistics confirm a narrow, nearly symmetric distribution with occasional low-pressure, high-flux excursions captured in the upper tail. Figure 1 confirms that the cleaning and gap–filling procedure preserves the intrinsic spread of the data: the probability-density function (pdf, red) retains its narrow, quasi-Gaussian core, while the cumulative distribution (cdf, blue) still reproduces the modest right-hand tail associated with low-pressure, high-flux episodes. The removed outliers (¿10σ) fall well outside the plotted range, and the ¡0.2% of values reconstructed by the random-forest imputer lie comfortably within the central envelope.

In parallel, in-situ trace-gas measurements (CH_4 dry-air mole fractions and O_3) were obtained from the Jungfraujoch High-Alpine Research Station (46°33' N, 7°59' E), operated by the Climate and Environmental Physics division of the University of Bern. The primary station sits at 3450 m a.s.l. between the Jungfrau (4158 m) and Mönch (4099 m) peaks, while a second monitoring site—the Sphinx laboratory at 3580 m a.s.l., built in 1937—houses the continuous in-situ analysers used in this study (see https://www.climate.unibe.ch/services/

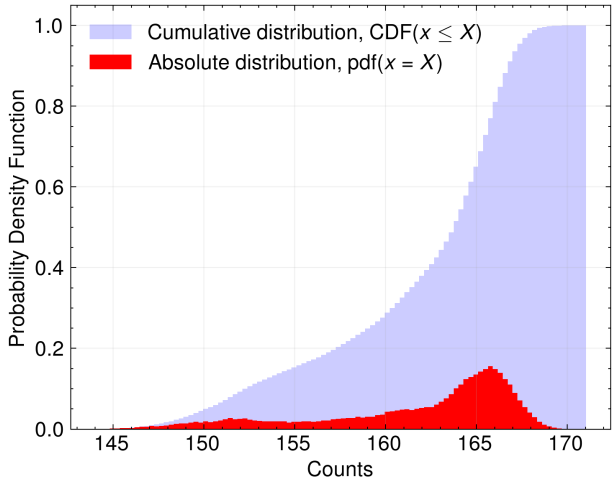

Figure 1: Empirical distribution of pressure-corrected hourly cosmic-ray counts at Jungfraujoch (2016–2024) after removal of $> 10\sigma$ detector artefacts and iterative random-forest imputation. The red bars depict the probability-density function, while the blue shading shows the cumulative distribution. The sharply bounded core (inter-quartile range 159–166 counts h^{-1}) and the modest right-tail extremes demonstrate that the minimalist cleaning strategy has not distorted the natural variability of the series.

services_of_cep/jungfraujoch_research_station). All three records span in the same interval that cosmic rays data on January 2016–December 2024 with nominal 1 h resolution. All three hourly series—cosmic–ray counts, CH_4, and O_3—were first merged into a single database covering 01:00 UTC on 1 January 2016 through 00:00 UTC on 1 July 2024. The harmonised database thus contains **74 328** common timestamps (01:00 UTC on 1 Jan 2016 to 00:00 UTC on 1 Jul 2024) with strict hour-by-hour synchronisation across the three variables. Isolated gaps shorter than three consecutive hours ($< 0.2\,\%$ of the grid) were bridged by linear interpolation, whereas longer gaps were reconstructed with the iterative random–forest imputation scheme detailed above. No additional rows were discarded, so the three records preserve identical lengths and strict hour-by-hour correspondence.

Let r_i denote the raw hourly record (counts or mixing ratio). After log-transform (for gases), removal of the seasonal component via a 30-day Lanczos high-pass, and z-standardisation, we obtain zero-mean, unit-variance anomalies

$$x_i = \frac{r_i^{(\log)} - S_i - \langle r^{(\log)} - S \rangle}{\sigma}, \qquad \langle x \rangle \approx 0, \quad \mathrm{Var}(x) = 1. \tag{1}$$

MFDFA/MFDCCA operate on the cumulative profile

$$Y(j) = \sum_{i=1}^{j} [x_i - \langle x \rangle] \approx \sum_{i=1}^{j} x_i, \tag{2}$$

which is *not* constrained to have zero mean even if x_i does. Hence, the right panels of Fig. 2 display the cumulative profiles $Y(j)$ (standardised, arbitrary units), while the left panels show the native observations (physical units).

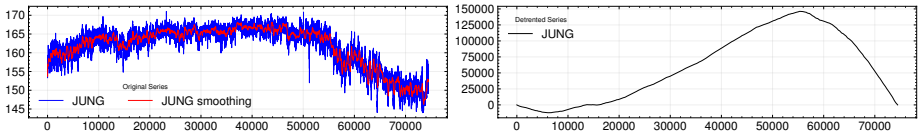

(a) Cosmic-ray counts (JUNG)

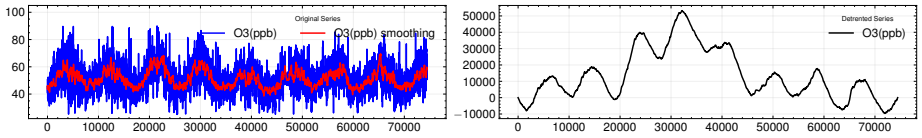

(b) O_3 mixing ratio

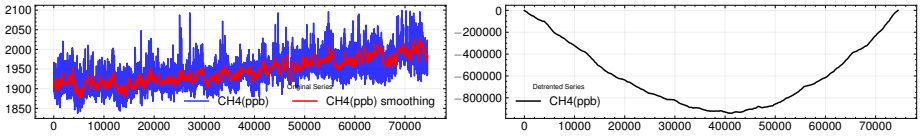

(c) CH_4 mixing ratio

Figure 2: Hourly time series at Jungfraujoch (2016–2024). Left subpanels: raw observations (physical units) and 30-day Lanczos smoother (black). Right subpanels: *cumulative profiles* $Y(j) = \sum_{i=1}^{j} x_i$ of the standardised anomalies used in MFDFA/MFDCCA (arbitrary units). Note that x_i is zero-mean by construction, but $Y(j)$ need not be centred; scales therefore differ between left and right panels and are not meant for direct comparison. Units are counts h^{-1} for cosmic rays and ppb for O_3 and CH_4. All three records are synchronised on the common timeline described in Sect. 2.1.

Figure 2 provides an overview of the three synchronised hourly records analysed in this study. Panel 2(a) confirms that the pressure–corrected cosmic-ray monitor at Jungfraujoch registers only modest variability: the raw counts oscillate within a narrow ∼25-count band over the entire 8.5-year period, and the 30-day Lanczos curve (black line) is virtually featureless apart from the well-known ∼11-year solar modulation trend that lowers the flux after 2020. By contrast, Panel 2(b) shows that lower-stratospheric O_3 mixing ratios exhibit a pronounced annual cycle with springtime maxima and late-summer minima, superposed on interannual excursions of 10–15 ppb linked to dynamical variability. Panel 2(c) reveals a gradual upward drift in CH_4 of $\approx 7\,\mathrm{ppb\,yr^{-1}}$—consistent with global trends reported by NOAA—and a clear quasi-seasonal envelope driven by tropopause height and regional transport.

The right sub-panels in each frame display the cumulative profiles $Y(j)$ of the standardised anomalies used in the multifractal analysis, whereas the left sub-panels show the raw observations and a 30-day smoother. For cosmic rays, the anomalies cluster tightly around zero and highlight the occasional high-flux excursions associated with low-pressure systems. O_3 anomalies emphasise episodic drops during late-winter stratospheric warmings, whereas CH_4 anomalies isolate synoptic pulses tied to meridional advection. Taken together, Fig. 2 illustrates that the three series share common intra-monthly variability but differ markedly in their longer-term behaviour—an ideal configuration for probing scale-dependent cross-correlations with the multifractal tools introduced in Sect. 2.

2.2. Multifractal framework

Standard linear correlation or Fourier methods cannot disentangle non-stationary, scale-variant couplings. We therefore adopt the multifractal detrended fluctuation family introduced by Kantelhardt et al. (2002) and its bivariate extensions (Podobnik and Stanley, 2008; Zebende and da Silva Filho, 2018).

Role of q versus scale s. In all multifractal detrended methods, the fluctuation *order q* controls *amplitude sensitivity*, whereas the window length s controls the *time scale* being probed. Negative orders ($q < 0$) overweight small fluctuations, while positive orders ($q > 0$) emphasise large excursions; $q = 0$ yields a logarithmic average (Kantelhardt et al., 2002; Gorjão et al., 2022). Therefore, statements about "$q \leq 0$" pertain to behaviour *conditional on small-to-moderate amplitudes*, not to a specific time scale. Time-scale localisation arises from s: for instance, $s \approx$ 24–168 h targets 1–7 day variability, whereas $s \approx$ 168–720 h targets 7–30 day variability. Our interpretation combines these two axes: we assess persistence for a given amplitude class (via q) *within* chemically motivated scale bands (via s).

2.2.1. Multifractal Detrended Fluctuation Analysis

For a zero-mean series x_i ($i = 1, \ldots, N$) the cumulative profile is $Y(j) = \sum_{i=1}^{j} [x_i - < x >]$. The profile is divided into $2N_s$ non-overlapping segments of length s (we use 18 logarithmically spaced scales, s = 8–4096 h). In each segment ν we fit and subtract a fifth-order polynomial $P_\nu^{(5)}$, then compute the variance (Gorjão et al., 2022; Oświęcimka et al., 2014)

$$F_\nu^2(s) = \frac{1}{s} \sum_{k=1}^{s} \left[Y((\nu - 1)s + k) - P_\nu^{(5)}(k) \right]^2 . \tag{3}$$

Following Zhou (2008), we compute the algebraic mean

$$\mu_q(s) = \frac{1}{2N_s} \sum_{\nu=1}^{2N_s} \operatorname{sign}\left(F_\nu(s)\right) \left| F_\nu(s) \right|^{q/2}, \tag{4}$$

and define, for $q \neq 0$,

$$F_{\nu,q}(s) = \operatorname{sign}\left(\mu_q(s)\right) \left| \mu_q(s) \right|^{1/q}. \tag{5}$$

For $q = 0$ we use the log-average of absolute values,

$$F_{\nu,0}(s) = \exp\left\{ \frac{1}{4N_s} \sum_{\nu=1}^{2N_s} \ln \left| F_\nu(s) \right| \right\}^{1/2} . \tag{6}$$

In Sierra-Porta (2025); Sierra-Porta and Domínguez-Monterroza (2022) a different normalisation was adopted for a specific coefficient; here we use the signed-power formalism of Zhou (2008) (see also Zebende and da Silva Filho, 2018) to retain the algebraic sign of cross-correlations at all scales.

Power-law scaling (Molino-Minero-Re et al., 2015), $F_q(s) \propto s^{h(q)}$, defines the *generalised Hurst exponent* $h(q)$ (Ellis, 2007; Mielniczuk and Wojdyłło, 2007):

- $h(q) \simeq 0.5$: uncorrelated (white) noise.

- $h(q) < 0.5$: anti-persistent, short-range correlations dominate; small increments tend to be followed by opposite-sign increments.
- $0.5 < h(q) < 1$: persistent, long-range correlations; increments favour the same sign over many lags (e.g. fractional Gaussian noise).
- $h(q) \geq 1$: non-stationary, trending behaviour akin to fractional Brownian motion.

Multifractality manifests when $h(q)$ varies with q. The Legendre transform gives the *singularity spectrum* $\alpha = h(q) + q\,h'(q)$ and its fractal dimension $f(\alpha) = q[\alpha - h(q)] + 1$. Here α (the Hölder exponent) measures the intensity of local fluctuations, and $f(\alpha)$ describes the Hausdorff dimension of the subset of points that share the same α. A broad spectrum $\Delta\alpha = \alpha_{\max} - \alpha_{\min}$ indicates strong multifractality, whereas $\Delta\alpha \to 0$ collapses to monofractal (single-scale) behaviour.

In Sect. 3 we report $h(q)$, α and $f(\alpha)$ for each variable and interpret the results in terms of turbulence, transport and ion-chemistry regimes relevant to Jungfraujoch.

2.2.2. *Multifractal Detrended Cross-Correlation Analysis*

To diagnose scale-dependent couplings between two pre-processed series x_i and y_i ($i = 1, \ldots, N$) we employ the bivariate extension of MFDFA (Podobnik and Stanley, 2008; Zebende and da Silva Filho, 2018), retaining *exactly* the same configuration used above ($s \in \{8, \ldots, 4096\}$ h, $q \in [-5, 5]$, fifth-order detrending, dual segmentation).

Profiles and local cross-variances. Define the cumulative profiles $X(j) = \sum_{i=1}^{j}[x_i - < x >]$, $Y(j) = \sum_{i=1}^{j}[y_i - < y >]$. For each window length s the profiles are divided into $2N_s$ non-overlapping segments, detrended with the same fifth-order polynomial fit $P^{(5)}_{\nu,X}$ and $P^{(5)}_{\nu,Y}$, and the *local cross-covariance* is

$$F_{\nu,xy}(s) = \frac{1}{s}\sum_{k=1}^{s}\Big[X((\nu-1)s+k) - P^{(5)}_{\nu,X}(k)\Big]\Big[Y((\nu-1)s+k) - P^{(5)}_{\nu,Y}(k)\Big]. \tag{7}$$

Signed-q aggregation for cross-fluctuations. Let

$$\mathcal{S}_{q/2}\{Z_\nu\} = \frac{1}{2N_s}\sum_{\nu=1}^{2N_s}\operatorname{sgn}(Z_\nu)\,|Z_\nu|^{q/2}$$

denote the signed power–mean of order $q/2$ (Zhou, 2008). Applied to the local cross–covariances $Z_\nu \equiv F_{\nu,xy}(s)$, the *bivariate* fluctuation function is

$$F_{xy,q}(s) = \operatorname{sgn}\!\big(\mathcal{S}_{q/2}\{F_{\nu,xy}(s)\}\big)\,\Big|\mathcal{S}_{q/2}\{F_{\nu,xy}(s)\}\Big|^{1/q}, \qquad q \neq 0, \tag{8}$$

which preserves the algebraic sign of cross–covariances while avoiding roots of negative arguments. For $q = 0$ we adopt the geometric mean of absolute values,

$$F_{xy,0}(s) = \exp\left\{\frac{1}{4N_s}\sum_{\nu=1}^{2N_s}\ln\Big|F_{\nu,xy}(s)\Big|\right\}^{1/2}. \tag{9}$$

Power-law scaling $F_{xy,q}(s) \propto s^{\lambda(q)}$ defines the *generalised cross-correlation exponent* $\lambda(q)$. For two independent white noises $\lambda(q) \approx 0.5$; $\lambda(q) > 0.5$ (< 0.5) signals persistent (anti-persistent) cross-correlations, with the degree of persistence increasing as $|\lambda(q) - 0.5|$.

Interpretation guide.

- $\lambda(q) \approx [h_x(q) + h_y(q)]/2$: the two series share a common multifractal structure but no additional cross-persistence.
- $\lambda(q) > [h_x(q) + h_y(q)]/2$: genuine long-range cross-correlations dominate, as expected if CR variability modulates gas chemistry at matching scales.

All calculations are executed with the `fathon` v3.1 Python package (Bianchi, 2020), ensuring consistency with the MFDFA implementation.

3. Results and discussions

A useful first benchmark is the conventional correlation matrix. Pearson's coefficient yields a moderate anticorrelation between cosmic-ray counts and CH_4 mixing ratios ($\rho = -0.47$), a virtually null relationship between JUNG and O_3 ($\rho = 0.02$), and a weak negative link between O_3 and CH_4 ($\rho = -0.11$). When rank information alone is considered, Spearman's r_s confirms the negligible JUNG–O_3 association ($r_s = 0.02$) and the weak O_3–CH_4 coupling ($r_s = -0.11$), but lowers the strength of the JUNG–CH_4 anticorrelation to ($r_s = -0.30$). The difference between the two metrics suggests that the cosmic-ray influence on methane is not strictly linear: extreme excursions contribute to covariance, whereas the overall monotonic dependence is weaker.

Taken together, these low or moderate coefficients indicate that any cosmic-ray imprint on trace gases is likely embedded in non-linear, scale-dependent dynamics—precisely the regime that multifractal methods are designed to unravel. The following sections therefore move beyond global correlations to a multifractal characterisation of each series and their cross-dependencies.

3.1. MFDFA results: Univariate multifractal structure

Figure 3 shows the log–log plots of the fluctuation function $F_q(s)$ versus window length s for five representative orders $q \in \{-5, -2.5, 0, 2.5, 5\}$. All three variables preserve clean power laws across the 8–4096 h band defined by the analysis grid, confirming that the chosen window range is appropriate. The cosmic-ray record (*JUNG*) exhibits only a modest spread in slopes, indicating scale invariance over nearly two decades. By contrast, both O_3 and CH_4 show visibly steeper lines at negative q and shallower ones at positive q, a hallmark of pronounced multifractality.

The near-parallel lines for cosmic rays are consistent with heliospheric modulation being the chief driver of variability: recurrent coronal-hole streams inject power near 27 d, while the 11–22 yr solar cycle shapes lower frequencies, together yielding a quasi–monofractal signature over the 8–4096 h window. For the trace gases, the widening fan of slopes at extreme q mirrors the mixture of rapid photochemical relaxation (hours–days for O_3, weeks for CH_4) and slower dynamical forcing (isentropic mixing, stratospheric intrusions) that amplifies small and large fluctuations differentially.

Figure 4 presents the generalised Hurst exponent $h(q)$. For cosmic rays, $h(q)$ oscillates narrowly around 1.10 ± 0.07, suggesting a near-monofractal, persistent—but stationary-differenced—process. O_3 and CH_4 exhibit pronounced curvature: $h(-5) \approx 1.35$–1.40 and $h(5) \approx 0.88$–0.90, giving $\Delta h \approx 0.45$. Values $h(q) > 1$ at negative q point to super-persistence of low-amplitude fluctuations, whereas the decline toward $h(q) \approx 0.9$ at positive q reveals weaker persistence—or incipient anti-persistence—during intense anomalies.

Physical note. Low-amplitude super-persistence in the gases matches the long chemical lifetimes of background CH_4 and the slow radiative–dynamical feedback that governs mid-latitude

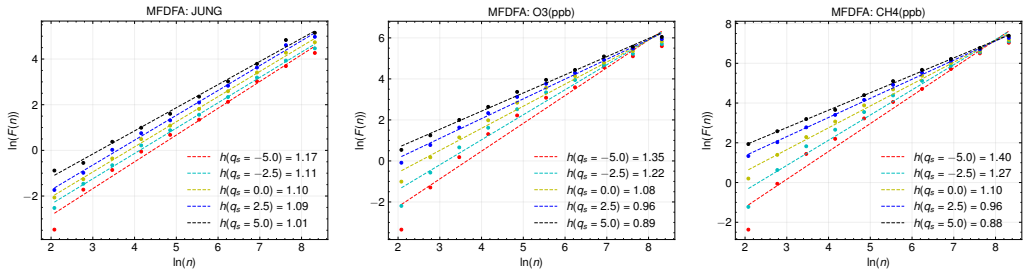

(a) JUNG (b) O_3 (c) CH_4

Figure 3: Multifractal fluctuation functions $F_q(s)$ for five fluctuation orders ($q = -5, -2.5, 0, 2.5, 5$). Linear segments spanning 8–4096 h certify robust scaling. The narrow bundle for cosmic rays contrasts with the fan-shaped envelopes for O_3 and CH_4, foreshadowing stronger multifractality in the gases.

O_3. Conversely, the soft drop in $h(q)$ for strong anomalies corresponds to episodic stratospheric intrusions, deep tropospheric mixing and sudden horizontal advection, all of which can rapidly erase sequential memory.

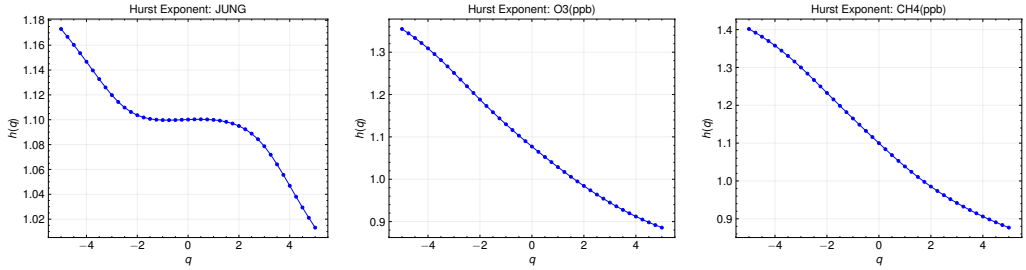

(a) JUNG (b) O_3 (c) CH_4

Figure 4: Generalised Hurst exponent $h(q)$ as a function of the fluctuation order q. A nearly flat curve for cosmic rays indicates weak multifractality, whereas the strongly curved spectra for O_3 and CH_4 imply heterogeneous scaling across amplitudes. Dashed lines mark the white-noise threshold $h(q) = 0.5$ and the fractional Brownian-motion threshold $h(q) = 1$.

Figure 5 plots the mass-exponent function $\tau(q) = q\,h(q) - 1$. For a perfect monofractal, $\tau(q)$ would be a straight line of slope h. The cosmic-ray curve (JUNG) is almost linear, confirming its near-monofractal nature, whereas both O_3 and CH_4 exhibit pronounced convexity, again signalling multifractality. The curvature is stronger for CH_4, implying a richer hierarchy of fluctuation amplitudes than in O_3.

Physical note. Convex $\tau(q)$ curves are characteristic of multiplicative cascades. In the trace gases, such cascades can arise from the interaction between episodic vertical transport and continuous chemical processing, while the flatter cosmic-ray line mirrors a single dominant source of variability—heliospheric modulation.

Figure 6 presents the singularity spectra $f(\alpha)$. Cosmic rays form a narrow, nearly symmetric parabola centred at $\alpha \approx 1.07$ with width $\Delta\alpha \simeq 0.16$, consistent with weak multifractality. O_3 broadens to $\Delta\alpha \simeq 0.36$, and CH_4 reaches $\Delta\alpha \simeq 0.48$, confirming that methane hosts the most

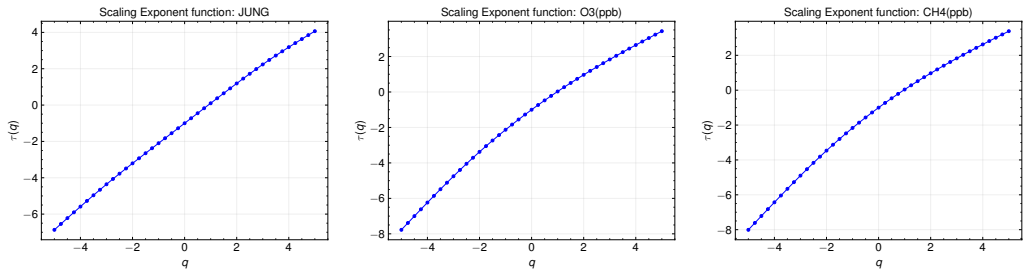

(a) JUNG (b) O_3 (c) CH_4

Figure 5: Scaling-exponent functions $\tau(q) = q\,h(q) - 1$. The cosmic-ray curve is nearly linear, whereas O_3 and CH_4 show pronounced convexity, a hallmark of strong multifractality.

heterogeneous set of scaling exponents.

Physical note. A wider spectrum implies that small and large fluctuations occupy geometrically distinct subsets of the time axis. For CH_4, the broadest $\Delta\alpha$ aligns with its dual control by slow hemispheric mixing (weeks to months) and rapid OH-driven loss (days), whereas O_3 sits between the highly persistent cosmic rays and the more variable methane, reflecting its intermediate chemical lifetime (1–2 weeks in the lower stratosphere).

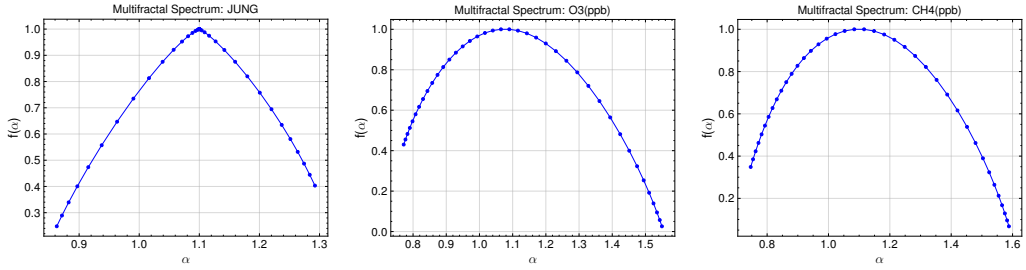

(a) JUNG (b) O_3 (c) CH_4

Figure 6: Singularity spectra $f(\alpha)$. The cosmic-ray spectrum is narrow and nearly parabolic, while O_3 and CH_4 exhibit progressively broader, asymmetric shapes, indicating increasingly heterogeneous scaling behaviour.

The singularity spectrum $f(\alpha)$ of a multifractal signal is commonly approximated by an inverted parabola $f(\alpha) = a\alpha^2 + b\alpha + c$. This quadratic captures three pieces of information in a single, compact form: (i) the peak location $\alpha_{\text{peak}} = -b/(2a)$, which marks the dominant Hölder exponent; (ii) the curvature a, whose magnitude gauges how rapidly the fractal dimension drops away from the peak; and (iii) the spectral width $\Delta\alpha$, a quantitative measure of multifractality. We performed least-squares fits to each empirical spectrum and derived two width metrics: the full span $\Delta\alpha = \alpha_{\max} - \alpha_{\min}$ i.e., from $q = +5$ to $q = -5$, and the half-maximum width (α distance between the two points where the parabola falls to $f_{\text{peak}}/2$). Table 1 summarises the results.

For GCR the fit explains 98 % of the spectral variance ($R^2 = 0.979$). Its sharp curvature ($a = -14.7$) and narrow half-max width (0.36) confirm that the cosmic-ray signal is almost monofractal: fluctuations cluster tightly around $\alpha_{\text{peak}} = 1.093$, consistent with the single-driver picture dominated by heliospheric modulation. The modest full span $\Delta\alpha = 0.43$ matches the

visual impression of the narrow $f(\alpha)$ curve in Fig. 6 a.

Methane displays the broadest spectrum ($\Delta\alpha = 0.84$; half-max width 0.68) and a shallower curvature ($a = -4.31$). The high goodness of fit ($R^2 = 0.995$) shows that a quadratic still captures the overall form, yet the gentle curvature implies a wide range of scaling exponents. This breadth is physically plausible: CH_4 variability reflects the interplay of long chemical lifetimes (weeks) and sporadic, short-lived loss bursts tied to OH peaks, modulated by both synoptic transport and hemispheric mixing. Ozone occupies an intermediate regime: $\Delta\alpha = 0.78$ and a half-max width of 0.64, with curvature $a = -4.85$ and $R^2 = 0.995$. Its peak at $\alpha_{\text{peak}} = 1.100$ is close to the cosmic-ray value, reflecting persistent behaviour, but the wider spectrum points to additional processes—photochemical production and loss, tropopause folds, and stratospheric intrusions—that broaden the scaling hierarchy relative to cosmic rays yet remain narrower than for CH_4.

These quadratic metrics reinforce the conclusions drawn from $h(q)$ and $\tau(q)$: cosmic rays are almost monofractal, O_3 shows moderate multifractality, and CH_4 is the most heterogeneous. The increasing spectral width from JUNG $\rightarrow$ O_3 $\rightarrow$ CH_4 mirrors the growing complexity of the underlying atmospheric processes—ranging from a single heliospheric driver to multi-scale chemical–dynamical couplings. In Sect. 3.2 we test whether any portion of this broad gas spectrum locks onto the cosmic-ray variability through scale-dependent cross-correlations.

Table 1: Quadratic fit parameters for the singularity spectra.

Series	a	b	c	$\Delta\alpha$ (full / half-max)
JUNG	−14.72	32.18	−16.62	0.43 / 0.36
O_3	−4.85	10.67	−4.87	0.78 / 0.64
CH_4	−4.31	9.67	−4.41	0.84 / 0.68

The cosmic-ray series is nearly monofractal—well described by a single-memory fractional Brownian process driven chiefly by heliospheric modulation—whereas O_3 and, more markedly, CH_4 exhibit broad, asymmetric $f(\alpha)$ spectra that demand a continuum of scaling exponents. This multifractality points to the superposition of photochemical relaxation, vertical transport, and synoptic advection that sharpen or dampen variability in different amplitude bands. These contrasts set up the bivariate stage: Sect. 3.2 examines whether any scale-specific fluctuation regime in the gases mirrors a physically plausible imprint of cosmic-ray forcing via HO_x/NO_x chemistry and other space-weather pathways.

3.2. Cross–scale coupling: MFDCCA results

Figure 7 plots $\ln F_{xy,q}(s)$ versus $\ln s$ for five representative orders ($q = -5, -2.5, 0, 2.5, 5$). Both cross-pairs—CH_4–JUNG and O_3–JUNG—retain clean power laws throughout the 8–4096 h window, validating the same scaling domain used in the univariate analysis. Slope estimates extracted from the straight-line segments yield the generalised cross-Hurst exponents $h_{xy}(q)$:

Pair	$h_{xy}(-5)$	$h_{xy}(-2.5)$	$h_{xy}(0)$	$h_{xy}(2.5)$	$h_{xy}(5)$
CH_4–JUNG	1.19	1.14	1.10	1.06	1.01
O_3–JUNG	1.18	1.13	1.08	1.05	1.02

Figure 8 shows $h_{xy}(q)$ for each pair. Both curves decline smoothly with q, remaining > 1 at negative and small positive orders and approaching unity at the largest amplitudes. This behaviour indicates strong, super-persistent cross-correlations for small-to-moderate fluctuations, but a weakening coupling for the most extreme events.

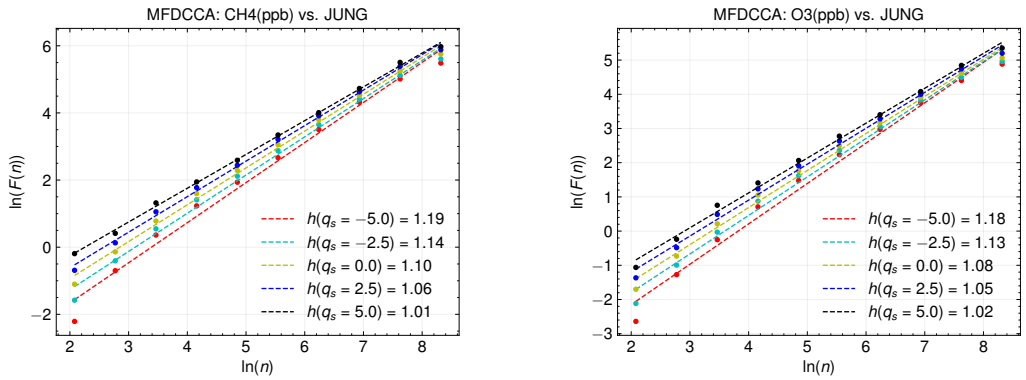

(a) CH_4–JUNG (b) O_3–JUNG

Figure 7: Log–log fluctuation functions $F_{xy,q}(s)$ for two cross–variable pairs and five fluctuation orders. Linear behaviour across 8–4096 h confirms robust power-law scaling.

Quantitatively, for O_3–JUNG we find $h_{xy}(q) = 1.18, 1.13, 1.08$ at $q = -5, -2.5, 0$, respectively, while for CH_4–JUNG the corresponding values are 1.19, 1.14, 1.10, all declining toward ~ 1.0 for $q = 5$ (Fig. 8).

Cross–Hurst values in the range 1.05–1.20 for $q \leq 0$ imply that small to moderate anomalies in CH_4 and O_3 fluctuate in lock-step with cosmic-ray intensity over multi-day to fortnight scales—compatible with the 1–7 d (O_3) and 7–30 d (CH_4) chemical response windows of the HO_x/NO_x pathway discussed in Sect. 1. The approach of $h_{xy}(q)$ to 1.0 for $q \geq 2.5$ suggests that large, impulsive gas excursions (e.g. stratospheric intrusions, deep convection) decouple from cosmic-ray forcing and are dominated instead by dynamical processes.

While the cross–Hurst spectra demonstrate scale-dependent persistence, they do not encapsulate the full cross-scaling geometry. We therefore turn to the cross–mass exponents $\tau_{xy}(q)$ and the joint singularity spectra $f_{xy}(\alpha)$ to characterise the breadth and shape of the multifractal coupling.

Figure 9 presents the mass–exponent curves $\tau_{xy}(q) = q\,h_{xy}(q) - 1$ for the two cross–variable pairs. Because $\tau_{xy}(q)$ is concave, both pairs qualify as multifractally cross-correlated. Convexity is slightly stronger for CH_4–JUNG than for O_3–JUNG, mirroring the broader univariate spectrum of CH_4. At large positive q the curves approach—but do not cross—the monofractal reference line $\tau(q) = q - 1$, indicating that even the most intense joint fluctuations retain some multifractal structure.

Figure 10 displays the joint spectra $f_{xy}(\alpha)$. Both cross–spectra are well described by inverted parabolas, as signalled by their negative quadratic coefficients ($a < 0 \Rightarrow \mathrm{d}^2 f/\mathrm{d}\alpha^2 = 2a < 0$): they are therefore concave–down and centred on a single dominant singularity. The larger magnitude of a in the O_3–JUNG fit ($|a| = 14.8$ vs. 13.4 for CH_4–JUNG) implies a steeper curvature and, consequently, a tighter clustering of α values around the peak, whereas the shallower curvature for CH_4–JUNG allows the spectrum to spread over a wider α range. In both cases the peak Hölder exponent falls near $\alpha \approx 1.10$, indicating strongly persistent joint fluctuations.

The quadratic–fit diagnostics then refine the multifractal comparison. For the CH_4–JUNG pair the fitted parabola $f_{xy}(\alpha) = -13.37\,\alpha^2 + 29.40\,\alpha - 15.17$ captures 99.8 % of the spectral variance ($R^2 = 0.9976$). The vertex sits at $\alpha_{\mathrm{peak}} = 1.0996$ with $f_{\mathrm{peak}} = 0.9908$; the full spectral width is $\Delta\alpha_{\mathrm{full}} = 0.4163$, and the half–maximum width is $\Delta\alpha_{1/2} = 0.3850$.

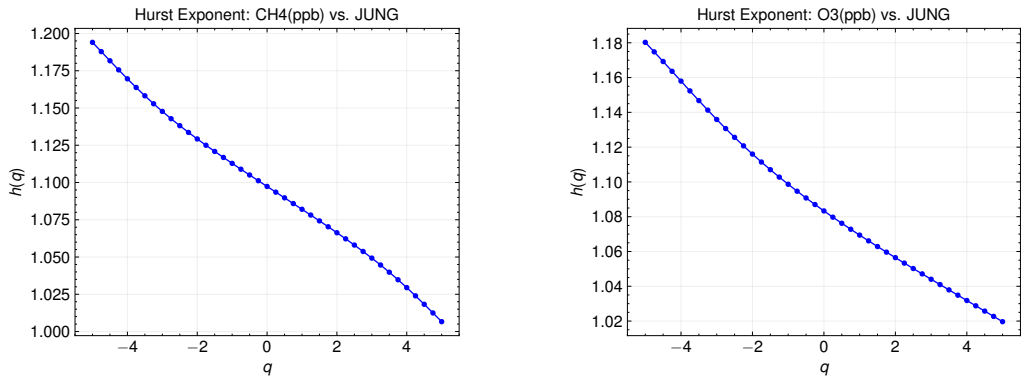

(a) CH_4–JUNG (b) O_3–JUNG

Figure 8: Cross–Hurst exponent $h_{xy}(q)$ as a function of fluctuation order q. Values exceeding unity signify super-persistent cross-correlations; the gradual decline toward 1.0 at large q implies weaker coupling for the most intense excursions.

For the O_3–JUNG pair the best–fit curve $f_{xy}(\alpha) = -14.80\,\alpha^2 + 32.37\,\alpha - 16.70$ explains 99.2 % of the variance ($R^2 = 0.9916$). Its peak lies at $\alpha_{\text{peak}} = 1.0935$ with $f_{\text{peak}} = 0.9934$; the spectrum is narrower, $\Delta\alpha_{\text{full}} = 0.3222$. Because the parabola drops below half its peak outside the observed α range, a meaningful half–maximum width cannot be defined for this pair.

In sum, the CH_4–JUNG cross-spectrum is broader and more heterogeneous, whereas the O_3–JUNG spectrum clusters more tightly around its peak—consistent with methane's longer chemical memory and more varied transport pathways compared with lower–stratospheric ozone. The larger spread for CH_4–JUNG indicates that methane responds to cosmic-ray variability across a broader hierarchy of fluctuation intensities than does ozone, consistent with the longer chemical lifetime and more diverse transport pathways of CH_4.

The broader CH_4–JUNG cross-spectrum suggests that cosmic-ray ionisation influences methane variability over a wider amplitude range, likely because CH_4 integrates both slow background oxidation and episodic OH bursts triggered by NO_x injections. Ozone, with a shorter lower-stratospheric lifetime, shows a more modest multifractal coupling—strong at small-to-moderate amplitudes but damped for the largest anomalies that are dominated by dynamical events such as stratospheric intrusions. Together with the cross–Hurst analysis, these spectra reinforce the view that cosmic-ray forcing imprints scale-dependent structure on both trace gases, yet its relative importance diminishes as one moves toward the most extreme excursions of each series.

3.3. Origins of multifractality and implications

The univariate MFDFA results show a clear hierarchy: cosmic-ray counts are almost monofractal, with a narrow $f(\alpha)$ peaked near $\alpha \approx 1.10$; ozone exhibits moderate multifractality, and methane the broadest, most asymmetric spectrum. This progression reflects the number and time-scale diversity of the underlying processes: cosmic rays are governed chiefly by heliospheric modulation, whereas O_3 and CH_4 integrate photochemistry, vertical transport and synoptic advection, each operating on different amplitude bands.

Cross–Hurst exponents $h_{xy}(q) > 1$ for $q \leq 0$ indicate that *small-to-moderate amplitude* anomalies in the gases fluctuate persistently and in phase with cosmic rays *within* specific scale

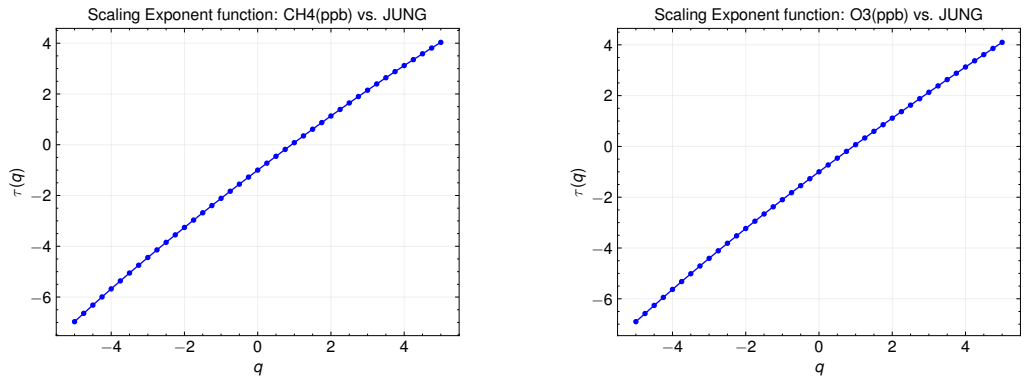

(a) CH_4–JUNG (b) O_3–JUNG

Figure 9: Cross–mass exponent functions $\tau_{xy}(q)$. The convex deviation from the monofractal line $\tau = q - 1$ (grey, not shown) confirms multifractal cross-correlations, stronger for CH_4–JUNG than for O_3–JUNG.

bands. In particular, for O_3 the persistence is most evident at $s \approx 24$–168 h (1–7 days), whereas for CH_4 it shifts toward $s \approx 168$–720 h (7–30 days), matching the HO_x/NO_x latency windows discussed in Sect. 1. By contrast, for large excursions ($q \gtrsim 2.5$) $h_{xy}(q) \to 1$, consistent with dynamical events dominating the variance.

Quadratic fits to the cross-spectra quantify these differences. CH_4–JUNG displays a wider width ($\Delta\alpha_{\text{half}} = 0.39$) than O_3–JUNG ($\Delta\alpha_{\text{half}} < 0.33$), implying that methane responds to cosmic-ray variability over a richer amplitude hierarchy, plausibly because its longer chemical lifetime allows both slow background oxidation and episodic OH bursts to register the ionisation signal. Ozone, with shorter memory, couples to cosmic rays mainly in the low-to-moderate fluctuation regime.

These findings suggest that cosmic-ray forcing leaves a scale-selective fingerprint on lower-stratospheric chemistry: detectable but modest relative to transport-driven extremes. Linear correlation underplays this imprint, whereas multifractal diagnostics expose the hidden persistence shared between ionisation and gas variability on multi-day horizons. Future predictive models—especially those targeting sub-monthly O_3 and CH_4 anomalies—could therefore benefit from incorporating cosmic-ray flux as a multiscale covariate rather than a simple linear predictor. At the same time, the narrowing of cross-spectra for large excursions underscores that space-weather forcing is a second-order player once strong dynamical events dominate the budget.

The multifractal framework used here (i) remains robust under strong trends and long-range persistence, (ii) separates amplitude classes via q while resolving time scales via s, and (iii) enables a physics-based interpretation by aligning scale bands with independent, chemically motivated latency windows (1–7 d for O_3, 7–30 d for CH_4). This combination reveals scale-selective couplings that are largely invisible to linear, single-scale diagnostics.

4. General conclusions

Our multifractal analysis of eight and a half years (2016–2024) of hourly cosmic-ray counts together with co-located O_3 and CH_4 measurements at Jungfraujoch yields four main insights.

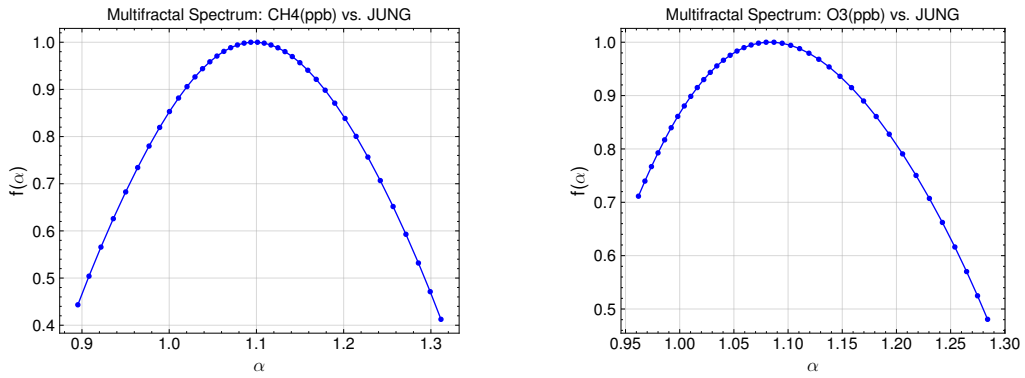

(a) CH_4–JUNG (b) O_3–JUNG

Figure 10: Cross-singularity spectra $f_{xy}(\alpha)$. Both spectra peak near $\alpha \approx 1.10$, but the CH_4–JUNG pair displays a noticeably broader width, signalling a richer hierarchy of joint fluctuation strengths.

First, a clear hierarchy emerges: cosmic rays are essentially monofractal, ozone displays moderate multifractality, and methane shows the broadest, most asymmetric $f(\alpha)$ spectrum—an ordering that mirrors the increasing diversity of underlying physical and chemical processes. **Second**, the MFDCCA results reveal a scale-selective ionisation coupling that is strongest for small-to-moderate fluctuation orders. For O_3–JUNG, the cross–Hurst exponents remain above unity ($h_{xy}(q) \approx 1.08$–1.18 for $q \in \{-5, -2.5, 0\}$), consistent with a persistent, in-phase joint variability on multi-day horizons that aligns with the chemically expected 1–7 day response window (Fig. 8). For CH_4–JUNG, the same pattern holds with slightly larger values at negative q ($h_{xy}(q) \approx 1.10$–1.19), in agreement with the longer 7–30 day methane response times. As q increases ($q \gtrsim 2.5$), $h_{xy}(q)$ approaches unity, indicating that the largest excursions in both gases are governed primarily by dynamical processes rather than by ionisation, in line with the narrower high-amplitude wings of the cross-singularity spectra in Fig. 10. **Third**, quadratic fits to the cross-spectra show that the CH_4–JUNG pair has a noticeably wider half-maximum width ($\Delta\alpha_{1/2} = 0.39$) than the O_3–JUNG pair ($\Delta\alpha_{1/2} < 0.33$), consistent with methane's longer chemical memory and more varied transport pathways. **Fourth**, standard Pearson and Spearman correlations miss much of this structure, whereas multifractal diagnostics uncover a modest yet persistent ionisation imprint at specific scales, suggesting that cosmic-ray flux could improve sub-monthly O_3 and CH_4 forecasts if included as a multiscale covariate rather than as a simple linear predictor.

Limitations.

- *Amplitude vs. scale localisation.* In multifractal detrended methods, the order q controls amplitude sensitivity, while the window length s controls time scale. Our interpretation of "small-to-moderate fluctuations" ($q \leq 0$) within chemically motivated scale bands (1–7 d for O_3, 7–30 d for CH_4) does not imply causality and cannot pinpoint specific events in time.

- *Single-site representativeness.* Results are based on one high-alpine station (Jungfraujoch). Spatial generality across latitudes, altitudes, and dynamical regimes remains to be established.

- *Preprocessing and configuration choices.* Detrending, polynomial order, scale range, and gap handling may influence exponents. Our sensitivity tests (alternative filters and STL) yielded exponent changes < 0.03, but residual dependence cannot be entirely excluded.

- *Confounding dynamical modes and events.* We did not explicitly control for large-scale variability (e.g., QBO, ENSO) or event-based forcings (e.g., Forbush decreases). These may modulate the amplitude and significance of scale-dependent couplings.

- *Measurement and correction uncertainties.* Residual barometric/thermal effects in neutron counts and trace-gas calibration uncertainties may add noise that slightly broadens the estimated spectra.

The present study is limited to a single high-alpine site; repeating the analysis at other latitudes and altitudes will help test the universality of the coupling. Incorporating indices of Forbush decreases and major dynamical modes (e.g., QBO, ENSO) would further disentangle the ionisation fingerprint from other stratospheric drivers. Cosmic rays leave a real but modulated signature on lower-stratospheric chemistry—strong enough to influence fine-scale variability in O_3 and CH_4, yet subordinate to the dominant dynamical pulses and tracer-specific chemical cycles.

Acknowledgments

We acknowledge the NMDB database www.nmdb.eu, founded under the European Union's FP7 programme (contract no. 213007) for providing data. Jungfraujoch neutron monitor data were kindly provided by the Physikalisches Institut, University of Bern, Switzerland. We gratefully acknowledge Dr. Martin Steinbacher and Dr. Stefan Reimann (Empa—Swiss Federal Laboratories for Materials Science and Technology) for providing the Jungfraujoch trace-gas data sets and for their helpful discussions on calibration and quality control. Their support was essential to the completion of this study.

References

Bianchi, S., 2020. fathon: A python package for a fast computation of detrendend fluctuation analysis and related algorithms. Journal of Open Source Software 5, 1828. doi:https://doi.org/10.21105/joss.01828.

Brune, W., Miller, D., Thames, A., Allen, H., Apel, E., Blake, D., Bui, T., Commane, R., Crounse, J., Daube, B., et al., 2020. Exploring oxidation in the remote free troposphere: Insights from atmospheric tomography (atom). Journal of Geophysical Research: Atmospheres 125, e2019JD031685. doi:https://doi.org/10.1029/2019JD031685.

Calisto, M., Usoskin, I., Rozanov, E., Peter, T., 2011. Influence of galactic cosmic rays on atmospheric composition and dynamics. Atmospheric Chemistry and Physics 11, 4547–4556. doi:https://doi.org/10.5194/acp-11-4547-2011.

Carslaw, K., Harrison, R., Kirkby, J., 2002. Cosmic rays, clouds, and climate. science 298, 1732–1737. doi:https://doi.org/10.1126/science.1076964.

Catone, D., Castrovilli, M.C., Nicolanti, F., Satta, M., Cartoni, A., 2023. Formation of h 3 o+ and oh by co 2 and n 2 o trace gases in the atmospheric environment. Physical Chemistry Chemical Physics 25, 25619–25628. doi:https://doi.org/10.1039/D3CP02427J.

Oświęcimka, P., Drożdż, S., Forczek, M., Jadach, S., Kwapień, J., 2014. Detrended cross-correlation analysis consistently extended to multifractality. Physical Review E 89, 023305. doi:https://doi.org/10.1103/PhysRevE.89.023305.

Christodoulakis, J., Varotsos, C., Mavromichalaki, H., Efstathiou, M., Gerontidou, M., 2019. On the link between atmospheric cloud parameters and cosmic rays. Journal of Atmospheric and Solar-Terrestrial Physics 189, 98–106. doi:https://doi.org/10.1016/j.jastp.2019.04.012.

Donnini, F., 2021. Cosmic ray nuclei: results from ams-02. Physics of Atomic Nuclei 84, 956–965. doi:https://doi.org/10.1134/S1063778821130081.

Ellis, C., 2007. The sampling properties of hurst exponent estimates. Physica A: Statistical Mechanics and its Applications 375, 159–173. doi:https://doi.org/10.1016/j.physa.2006.08.046.

Friis-Christensen, E., Svensmark, H., 1997. What do we really know about the sun-climate connection? Advances in Space Research 20, 913–921. doi:https://doi.org/10.1016/S0273-1177(97)00499-7.

Gong, S., Duan, L., Zhao, J., Wei, X., Feng, J., Li, Z., 2025. Temporal correlation between positive-charged cosmic ray flux and solar polar field variation: Insights from delayed modulation analysis. Physical Review D 111, 083050. doi:https://doi.org/10.1103/PhysRevD.111.083050.

Gorjão, L.R., Hassan, G., Kurths, J., Witthaut, D., 2022. Mfdfa: Efficient multifractal detrended fluctuation analysis in python. Computer Physics Communications 273, 108254. doi:https://doi.org/10.1016/j.cpc.2021.108254.

Grenfell, J.L., Grießmeier, J.M., von Paris, P., Patzer, A.B.C., Lammer, H., Stracke, B., Gebauer, S., Schreier, F., Rauer, H., 2012. Response of atmospheric biomarkers to no x-induced photochemistry generated by stellar cosmic rays for earth-like planets in the habitable zone of m dwarf stars. Astrobiology 12, 1109–1122. doi:https://doi.org/10.1089/ast.2011.0682.

Grenfell, J.L., Grießmeier, J.M., Patzer, B., Rauer, H., Segura, A., Stadelmann, A., Stracke, B., Titz, R., Von Paris, P., 2007. Biomarker response to galactic cosmic ray-induced no x and the methane greenhouse effect in the atmosphere of an earth-like planet orbiting an m dwarf star. Astrobiology 7, 208–221. doi:https://doi.org/10.1089/ast.2006.0129.

Harrison, R.G., Nicoll, K., Takahashi, Y., Yair, Y., 2015. Focus on high energy particles and atmospheric processes. Environmental Research Letters 10, 100201. doi:https://doi.org/10.1088/1748-9326/10/10/100201.

Holt, B., Benfer Jr, R.A., 2000. Estimating missing data: an iterative regression approach. Journal of Human Evolution 39, 289–296. doi:https://doi.org/10.1006/jhev.2000.0418.

Jackman, C.H., DeLand, M.T., Labow, G.J., Fleming, E.L., Weisenstein, D.K., Ko, M.K., Sinnhuber, M., Anderson, J., Russell, J.M., 2005. The influence of the several very large solar proton events in years 2000–2003 on the neutral middle atmosphere. Advances in Space Research 35, 445–450. doi:https://doi.org/10.1016/j.asr.2004.09.006.

Jackman, C.H., Marsh, D.R., Kinnison, D.E., Mertens, C.J., Fleming, E.L., 2016. Atmospheric changes caused by galactic cosmic rays over the period 1960–2010. Atmospheric Chemistry and Physics 16, 5853–5866. doi:https://doi.org/10.5194/acp-16-5853-2016.

Jackman, C.H., Marsh, D.R., Vitt, F.M., Garcia, R.R., Fleming, E.L., Labow, G.J., Randall, C.E., Lopez-Puertas, M., Funke, B., 2007. Short-and medium-term atmospheric effects of very large solar proton events. Atmospheric Chemistry and Physics Discussions 7, 10543–10588. doi:https://doi.org/10.5194/acpd-7-10543-2007.

Jeong, J., Oh, S., 2020. Seasonal variation of cosmic ray intensity observed by the oulu neutron monitor. Journal of Astronomy and Space Sciences 37, 165–170. doi:https://doi.org/10.5140/JASS.2020.37.3.165.

Kantelhardt, J.W., Zschiegner, S.A., Koscielny-Bunde, E., Havlin, S., Bunde, A., Stanley, H.E., 2002. Multifractal detrended fluctuation analysis of nonstationary time series. Physica A: Statistical Mechanics and its Applications 316, 87–114. doi:https://doi.org/10.1016/S0378-4371(02)01383-3.

Kirkby, J., Curtius, J., Almeida, J., Dunne, E., Duplissy, J., Ehrhart, S., Franchin, A., Gagné, S., Ickes, L., Kürten, A., et al., 2011. Role of sulphuric acid, ammonia and galactic cosmic rays in atmospheric aerosol nucleation. Nature 476, 429–433. doi:https://doi.org/10.1038/nature10343.

Konopka, P., Engel, A., Funke, B., Müller, R., Grooß, J.U., Günther, G., Wetter, T., Stiller, G., von Clarmann, T., Glatthor, N., et al., 2007. Ozone loss driven by nitrogen oxides and triggered by stratospheric warmings can outweigh the effect of halogens. Journal of Geophysical Research: Atmospheres 112. doi:https://doi.org/10.1029/2006JD007064.

Maghrabi, A., Alotaibi, R., Almutayri, M., Garawi, M., 2015. Influence of the atmospheric mass on the high energy cosmic ray muons during a solar cycle. Advances in Astronomy 2015, 939146. doi:https://doi.org/10.1155/2015/939146.

Maghrabi, A.H., Alzahrani, S.A., Alruhaili, A.S., 2023. The role of atmospheric pressure, temperature, and humidity on cosmic ray muons at a low latitude station. International Journal of Astronomy and Astrophysics 13, 236–258. doi:https://doi.org/10.4236/ijaa.2023.133014.

Maliniemi, V., Nesse Tyssøy, H., Smith-Johnsen, C., Arsenovic, P., Marsh, D.R., 2021. Effects of enhanced downwelling of no x on antarctic upper-stratospheric ozone in the 21st century. Atmospheric Chemistry and Physics 21, 11041–11052. doi:https://doi.org/10.5194/acp-21-11041-2021.

Marsh, N., Svensmark, H., 2000. Cosmic rays, clouds, and climate. Space Science Reviews 94, 215–230. doi:https://doi.org/10.1023/A:1026723423896.

Matthes, K., Funke, B., Andersson, M.E., Barnard, L., Beer, J., Charbonneau, P., Clilverd, M.A., Dudok de Wit, T., Haberreiter, M., Hendry, A., et al., 2017. Solar forcing for cmip6 (v3. 2). Geoscientific Model Development 10, 2247–2302. doi:https://doi.org/10.5194/gmd-10-2247-2017.

Meng, Z., Dabdub, D., Seinfeld, J.H., 1997. Chemical coupling between atmospheric ozone and particulate matter. Science 277, 116–119. doi:https://doi.org/10.1126/science.277.5322.116.

Mielniczuk, J., Wojdyłło, P., 2007. Estimation of hurst exponent revisited. Computational statistics & data analysis 51, 4510–4525. doi:https://doi.org/10.1016/j.csda.2006.07.033.

Miyahara, H., Kusano, K., Kataoka, R., Shima, S.i., Touber, E., 2023. Response of high-altitude clouds to the galactic cosmic ray cycles in tropical regions. Frontiers in Earth Science 11, 1157753. doi:https://doi.org/10.3389/feart.2023.1157753.

Molino-Minero-Re, E., García-Nocetti, F., Benítez-Pérez, H., 2015. Application of a time-scale local hurst exponent analysis to time series. Digital Signal Processing 37, 92–99. doi:https://doi.org/10.1016/j.dsp.2014.11.007.

Naik, V., Voulgarakis, A., Fiore, A.M., Horowitz, L.W., Lamarque, J.F., Lin, M., Prather, M.J., Young, P., Bergmann, D., Cameron-Smith, P., et al., 2013. Preindustrial to present-day changes in tropospheric hydroxyl radical and methane lifetime from the atmospheric chemistry and climate model intercomparison project (accmip). Atmospheric Chemistry and Physics 13, 5277–5298. doi:https://doi.org/10.5194/acp-13-5277-2013.

Nikfalazar, S., Yeh, C.H., Bedingfield, S., Khorshidi, H.A., 2020. Missing data imputation using decision trees and fuzzy clustering with iterative learning. Knowledge and Information Systems 62, 2419–2437. doi:https://doi.org/10.1007/s10115-019-01427-1.

Pierce, J., 2017. Cosmic rays, aerosols, clouds, and climate: Recent findings from the cloud experiment. Journal of Geophysical Research: Atmospheres 122, 8051–8055. doi:https://doi.org/10.1002/2017JD027475.

Podobnik, B., Stanley, H.E., 2008. Detrended cross-correlation analysis: A new method for analyzing two nonstationary time series. Physical review letters 100, 084102. doi:https://doi.org/10.1103/PhysRevLett.100.084102.

Portmann, R., Daniel, J., Ravishankara, A., 2012. Stratospheric ozone depletion due to nitrous oxide: influences of other gases. Philosophical Transactions of the Royal Society B: Biological Sciences 367, 1256–1264. doi:https://doi.org/10.1098/rstb.2011.0377.

Prather, M.J., Hsu, J., 2010. Coupling of nitrous oxide and methane by global atmospheric chemistry. Science 330, 952–954. doi:https://doi.org/10.1126/science.1196285.

Riádigos, I., González-Díaz, D., Pérez-Muñuzuri, V., 2022. Revisiting the limits of atmospheric temperature retrieval from cosmic-ray measurements. Earth and Space Science 9, e2021EA001982. doi:https://doi.org/10.1029/2021EA001982.

Satta, M., Catone, D., Castrovilli, M.C., Nicolanti, F., Cartoni, A., 2024. Ionic route to atmospheric relevant ho2 and protonated formaldehyde from methanol cation and o2. Molecules 29, 1484. doi:https://doi.org/10.3390/molecules29071484.

Scheucher, M., Grenfell, J.L., Wunderlich, F., Godolt, M., Schreier, F., Rauer, H., 2018. New insights into cosmic-ray-induced biosignature chemistry in earth-like atmospheres. The Astrophysical Journal 863, 6. doi:https://doi.org/10.3847/1538-4357/aacf03.

Schnadt, C., Dameris, M., Ponater, M., Hein, R., Grewe, V., Steil, B., 2002. Interaction of atmospheric chemistry and climate and its impact on stratospheric ozone. Climate Dynamics 18, 501–517. doi:https://doi.org/10.1007/s00382-001-0190-z.

Seinfeld, J.H., Pandis, S.N., 2016. Atmospheric Chemistry and Physics: From Air Pollution to Climate Change. 3 ed., Wiley.

Sierra-Porta, D., 2022. On the fractal properties of cosmic rays and sun dynamics cross-correlations. Astrophysics and Space Science 367, 116. doi:https://doi.org/10.1007/s10509-022-04151-5.

Sierra-Porta, D., 2025. Multifractal detrended cross-correlation coefficient for cosmic ray and sunspot time series. Journal of Atmospheric and Solar-Terrestrial Physics 266, 106407. doi:https://doi.org/10.1016/j.jastp.2024.106407.

Sierra-Porta, D., Domínguez-Monterroza, A.R., 2022. Linking cosmic ray intensities to cutoff rigidity through multifractal detrented fluctuation analysis. Physica A: Statistical Mechanics and its Applications 607, 128159. doi:https://doi.org/10.1016/j.physa.2022.128159.

Svensmark, H., Friis-Christensen, E., 1997. Variation of cosmic ray flux and global cloud coverage—a missing link in solar-climate relationships. Journal of atmospheric and solar-terrestrial physics 59, 1225–1232. doi:https://doi.org/10.1016/S1364-6826(97)00001-1.

Tabataba-Vakili, F., Grenfell, J., Grießmeier, J.M., Rauer, H., 2016. Atmospheric effects of stellar cosmic rays on earth-like exoplanets orbiting m-dwarfs. Astronomy & Astrophysics 585, A96. doi:https://doi.org/10.1051/0004-6361/201425602.

Tomassetti, N., Bertucci, B., Fiandrini, E., 2022. Temporal evolution and rigidity dependence of the solar modulation lag of galactic cosmic rays. Physical Review D 106, 103022. doi:https://doi.org/10.1103/PhysRevD.106.103022.

Utomo, Y., 2017. Correlation analysis of solar constant, solar activity and cosmic ray, in: Journal of Physics: Conference Series, IOP Publishing. p. 012045. doi:https://doi.org/10.1088/1742-6596/817/1/012045.

633 Varotsos, C., Golitsyn, G., Efstathiou, M., Sarlis, N., 2023a. A new method of nowcasting extreme cosmic ray events.
634 Remote Sensing Letters 14, 576–584. doi:https://doi.org/10.1080/2150704X.2022.2057204.
635 Varotsos, C., Golitsyn, G., Mazei, Y., Sarlis, N., Xue, Y., Mavromichalaki, H., Efstathiou, M., 2024. On the observed
636 time evolution of cosmic rays in a new time domain. Acta Astronautica 225, 436–443. doi:https://doi.org/10.
637 1016/j.actaastro.2024.09.034.
638 Varotsos, C., Golitsyn, G., Xue, Y., Efstathiou, M., Sarlis, N., Voronova, T., 2023b. On the relation between rain,
639 clouds, and cosmic rays. Remote Sensing Letters 14, 301–312. doi:https://doi.org/10.1080/2150704X.
640 2023.2190468.
641 Zebende, G., da Silva Filho, A., 2018. Detrended multiple cross-correlation coefficient. Physica A: Statistical Mechanics
642 and its Applications 510, 91–97. doi:https://doi.org/10.1016/j.physa.2018.06.119.
643 Zhou, W.X., 2008. Multifractal detrended cross-correlation analysis for two nonstationary signals. Physical Review
644 E—Statistical, Nonlinear, and Soft Matter Physics 77, 066211. doi:https://doi.org/10.1103/PhysRevE.77.
645 066211.